LANGMUIR

pubs.acs.org/Langmuir Article

Active Role of Vapor Clouds around Evaporating Sessile Droplets in Microgravity: Marangoni Jets and Electroconvection

Sam Dehaeck, Alexey Y. Rednikov,* Hatim Machrafi, Alekos Ioannis Garivalis, Paolo Di Marco, Senthil Kumar Parimalanathan, and Pierre Colinet

Cite This: https://doi.org/10.1021/acs.langmuir.3c00689 Read Online

ACCESS | Metrics & More | Article Recommendations | Supporting Information

Downloaded via UNIV DE LIEGE on June 30, 2023 at 06:51:21 (UTC).
See https://pubs.acs.org/sharingguidelines for options on how to legitimately share published articles.

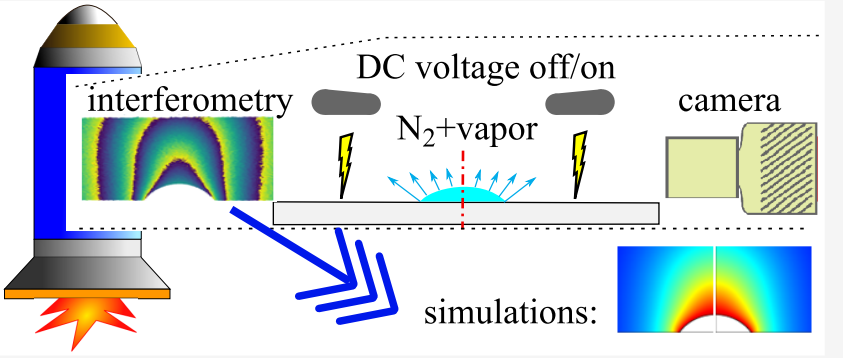

ABSTRACT: A benchmark microgravity experiment (dubbed "ARLES") is analyzed. It concerns evaporation of several-μL sessile droplets with a pinned millimetric circular contact line on a flat substrate into a vast calm (here nitrogen) atmosphere at nearly normal conditions. Hydrofluoroether (HFE-7100) is used as a working liquid whose appreciable volatility and heavy vapor accentuate the contrast between the micro- and normal gravity. A possibility of switching on a DC electric field (EF) of several kV/mm orthogonally to the substrate is envisaged. We here focus on the findings intimately associated with the visualization of the vapor cloud by means of interferometry and rationalized by means of extensive simulations. In particular, with different degrees of unexpectedness, we discover and explore a Marangoni jet (without EF) and electroconvection (with EF) in the gas, which would otherwise be masked by buoyancy convection. Using the same tools, we examine some malfunctions of the space experiment.

INTRODUCTION

The evaporation of a droplet deposited on a flat substrate is a common theme in many industrial contexts as spray cooling[1,2] and inkjet printing,[3] to cite but a few. Next to this industrial relevance, it also holds appeal for purely academic studies as a benchmark topic to study evaporation. This general appeal comes partly from the challenging couplings that exist in this configuration between liquid/solid[4−8] and liquid/gas.[9−11] These couplings are made all the more complex by the presence of the three phase contact line. This leads to a divergence near the contact line in e.g. the local mass transfer rate (leading to the coffee-ring effect[12,13]) and in the viscous stress generated by evaporation-induced currents (leading to evaporation-induced contact angles[14]).

In the present article, the focus will be on the vapor/liquid interaction and the marked differences in the dynamics of the vapor cloud when gravity is absent. Large differences are indeed expected in this case, as the presence of natural convection in the vapor cloud has already been described extensively in the literature for sessile droplets.[9,11,15−17] An especially strong enhancement of the evaporation rate, by a factor of 4 as compared to pure-diffusion simulations, was obtained[11] for a pendant droplet with a heavy vapor.

To explore evaporation of sessile droplets in microgravity, a sounding-rocket experiment ARLES (Advanced Research on Liquid Evaporation in Space) was conceived. The experiment involves both droplets of a pure liquid (Novec HFE-7100) and complex droplets with suspensions containing low concentration of nanoparticles in HFE-7100 evaporating into a nitrogen atmosphere at nearly normal conditions (28 °C and 1.051 mbar). Among the fundamental questions raised are the roles of Stefan flow and Marangoni flow (accentuated in microgravity, where no buoyancy effects are present) on the evaporation rate, vapor cloud distribution, possible role of an electric field as a forcing factor alternative to Earth's gravity,

Received: March 13, 2023
Revised: May 24, 2023

© XXXX American Chemical Society

Table 1. ARLES runs in the nomenclature of Kumar et al.[18a]

run name	g	U (kV)	volume range (μL)	measured J (μL/s)	measured J^* (−)	benchmark J^* (−)
1DP1g	1g	0	2.9→0.5	0.205	8.7	8.4[b]
2DP1gEF	1g	8	2.8→0.8	0.191	8.1	8.3[b]
3DP1g	1g	0	4.7→0.4	0.192	8.2	8.4[b]
4DP1gEF	1g	8	3.3→0.7	0.181	7.7	8.3[b]
6DPμgEF	0g	8	3.2→1.8	0.097	4.1	6.6[b]
7DPμg	0g	0	7.8→5.6	0.087	3.7	5.9[c]
8DPμgEF	0g	5.7	6.1→3.1	0.109	4.6	7.4[c]

[a]5DPμg discarded as deficient. Runs on ground (1g) and sounding rocket (0g). Voltage U applied. The range of the droplet volume V and the measured evaporation rate J (proving largely constant during a run) between the maximum injected volume and the volume at which the droplet either depins (1DP1g−6DPμgEF) or is flushed away (7DPμg and 8DPμgEF).[18] Cf. later on for more on the last two columns. J^* is J normalized to $10^9 D_g \rho_{sat,0} R_c/\rho_l$ = 0.02345 μL/s. Benchmark quasi-steady simulation results for comparison. Why such a big disagreement between experiment and theory in 0g is an issue under debate in the paper. [b]For V = 2.9 μL. [c]For V = 5.8 μL.

thermocapillary instabilities, and nanoparticle deposition patterns and self-assembly in microgravity. The launch was realized at Esrange (Sweden) in June 2019. Furthermore, shortly prior to that, a ground test campaign was carried out with the same setup. A more detailed description of the context/literature and experimental setup and a first analysis of the results are provided by Kumar et al.[18] and Garivalis et al.[19] This includes measurement of the droplet volume evolution from the side view and infrared diagnostics of the droplet from the top view. The volume is supposed to decrease due to the evaporation, and this is used to experimentally determine the evaporation rate. The infrared images are used,[18] among other things, to reveal thermocapillary instabilities in the droplet as well as to detect the moment the droplet depins from a groove of a radius of 2 mm where it finds itself pinned upon the injection. In the present paper, we rather focus on the findings made possible owing to vapor interferometry (cf. Dehaeck et al.[11]) in conjunction with numerical simulations. We shall deal with the pure-liquid cases without and with an electric field. The on-ground and in-flight experiment runs relevant here are summarized in Table 1, where the measured droplet volumes and evaporation rates are also provided following Kumar et al.[18] The in-flight (sounding rocket) runs were understandably quite unique due to limited time of the flight. In contrast, quite a number of runs have been performed on ground, and the ones chosen for Table 1 represent rather well the repeatability achieved.

The paper is organized as follows. In Experimental Setup, the key details of the ARLES setup that are relevant for the present study are provided. A first appreciation of the experimental results is given in First Results and Discussion, where a number of conjectures are made. This helped shaping the mathematical formulation described in Model. A full presentation of the experimental and simulation results together with an overall discussion are given in Further Results and Discussion, which is followed by Conclusions. A number of auxiliary details are relegated to Supporting Information.

EXPERIMENTAL SETUP

In the experiments, a pinned circular sessile droplet of 4 mm diameter is created on top of a 1" silicon wafer serving as the substrate (cf. Figure 1). The pinning is guaranteed by a groove (50 μm wide and deep, etched by Deep Reactive Ion Etching) in the wafer.[14,20] The wafer is thermally connected to a large metal block maintained at a "substrate" temperature T_{sub} = 28 °C. It is placed inside a 4-L axisymmetric chamber, as outlined in Figure 1. The chamber is filled initially with pure nitrogen at an "ambient" pressure p_{amb} = 105100 Pa.

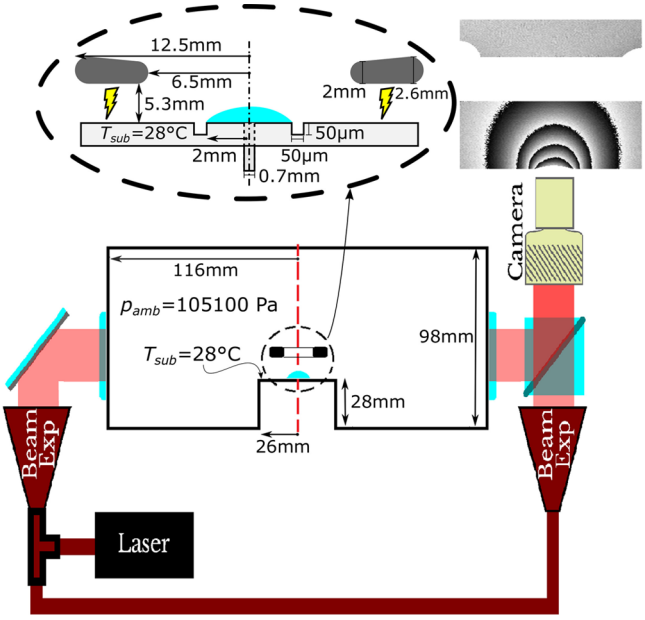

Figure 1. Schematic of the Mach−Zehnder interferometer and ARLES main evaporation cell (principally an axisymmetric geometry, not drawn to scale). Inset shows the details of the annular-ring electrode and evaporation site with a sessile droplet pinned on the groove. The (expanded) laser beam and the camera are used for both the side view and the vapor interferometry. The inset above the camera represents a (wrapped-phase) fringe pattern typical for the diffusion regime of evaporation (roughly hemispherical fringes), when gravity, Marangoni convection, and the electric field are either absent or not essential. The zones of the electrode and droplet are whitened out in the inset, and likewise in all fringe pictures hereafter.

The droplet is formed by pure Novec HFE-7100 liquid (cf. Table 2 for the properties) injected through a central hole with 0.7 mm diameter in the wafer. Also note that a washer-shaped (annular-ring) electrode is placed axisymmetrically at a 5.3 mm standoff distance from the substrate. Due to its relatively large central opening (13 mm), its geometrical influence on the evaporation rate of the droplet is expected to be minimal (as confirmed by benchmark simulations later on). At the same time, its possible electric influence (in the cases when a DC voltage U is applied between the electrode and the substrate) is one of the subjects of the present study.

In order to visualize the vapor cloud from a sessile droplet composed of pure HFE-7100 and evaporating into pure nitrogen, a Mach−Zehnder interferometer with a red diode laser (wavelength λ = 633 nm) was used.[11,25] Following the beam splitter, one part of the expanded laser beam passes in a parallel manner over the substrate with the sessile droplet (Figure 1). It is recombined with the other

https://doi.org/10.1021/acs.langmuir.3c00689
Langmuir XXXX, XXX, XXX−XXX

Table 2. Material Properties[a]

droplet contact radius	R_c	2 mm
ambient pressure	p_{amb}	105100 Pa
substrate temperature	T_{sub}	28 °C
universal gas constant	R_g	8.31 J/mol K
gas molar density	n_g	$p_{amb}/R_g(273.15\ K + T_{sub}) = 42.0\ mol/m^3$[b]
HFE-7100 molar mass	M_{HFE}	0.25 kg/mol
N_2 molar mass	M_{N_2}	0.028 kg/mol
saturation pressure at T_{sub}	$p_{sat,0}$	30385 Pa
saturation pressure	$p_{sat}(T)$	$p_{sat,0}e^{\mathcal{L}M_{HFE}(T-T_{sub})/Rg(273.15\ K+T_{sub})^2}$[c]
saturation molar fraction at T_{sub}	$\chi_{sat,0}$	$p_{sat,0}/p_{amb} = 0.289$[b]
saturation molar fraction	$\chi_{sat}(T)$	$\chi_{sat,0}e^{\mathcal{L}M_{HFE}(T-T_{sub})/Rg(273.15\ K+T_{sub})^2}$[c]
saturation vapor density at T_{sub}	$\rho_{sat,0}$	$p_{sat,0}M_{HFE}/R_g(273.15\ K + T_{sub}) = 3.03\ kg/m^3$[b]
latent heat of evaporation	$\mathcal{L}$	110.6 kJ/kg
gas density	$\rho_g(\chi)$	$n_g\ (M_{HFE}\ \chi + M_{N_2}(1-\chi))$[b]
vapor diffusion coefficient	D_g	$5.7 \times 10^{-6}\ m^2/s$[d]
N_2 dynamic viscosity	μ_{N_2}	1.79×10^{-5} Pa s
vapor dynamic viscosity	μ_{vap}	0.957×10^{-5} Pa s[e]
gas dynamic viscosity	$\mu_g(\chi)$	see Supporting Information
liquid density	ρ_l	$1474.8\ kg/m^3$
liquid dynamic viscosity	μ_l	0.000543 Pa s
surface tension	$\gamma(T)$	$13.6\ mN/m - \gamma_T\ (T - T_{sub})$
surface tension variation	γ_T	0.096 mN/K m[f]
liquid thermal conductivity	λ_l	0.06824 W/K m
liquid heat capacity	$c_{p,l}$	1189 J/kg K
gas refractive index increment	$\Delta n(\chi)$	0.00147χ[g]
laser wavelength	λ	633 nm
electric permittivity of vacuum	ϵ_0	8.8542×10^{-12} F/m
liquid dielectric permittivity	ϵ_l	7.39
gas dielectric permittivity	$\epsilon_g(\chi)$	$1 + 0.0455\chi$[h]

[a]Liquid: HFE-7100. Gas: N_2 + HFE-7100 vapor. HFE-7100 properties given according to 3M Novec online (unless indicated otherwise). Only γ and p_{sat} (and, hence, χ_{sat}) are considered as varying with T, the rest merely evaluated at T_{sub} (and p_{amb}) where relevant. [b]Ideal-gas approach. [c]Clausius−Clapeyron relation (partly linearized). [d]Fit of the 1 atm data[21] vs T, evaluated at $T = T_{sub}$, and recalculated by $D_g \sim p^{-1}$ at $p = p_{amb}$. [e]Linear interpolation of data.[22] [f]Cf., ref 23. [g]In-house measurement at 1 atm and 24 °C (agreeing well with Shevchenko et al.[21]) and recalculated by $\Delta n \sim \frac{p}{273.15\ K + T}$[24] at p_{amb} and T_{sub}. [h]For the lack of data, it is estimated by neglecting N_2 contribution against HFE vapor and assuming the same contribution per mole as for the liquid: $\frac{\epsilon_g - 1}{n_g \chi} = \frac{\epsilon_l - 1}{\rho_l / M_{HFE}}$.

part in the camera, yielding an interferometric pattern. A finite-fringe mode is used and the processing follows the method set forth elsewhere.[11,26,27] One obtains a so-called wrapped-phase image, as in Figure 1 (inset above the camera). The "phase" here is actually understood as the phase increment $\Delta\phi$ acquired by the beam due to the presence of the HFE-7100 vapor relative to the initial pure-nitrogen atmosphere. It is a planar field (defined in the plane orthogonal to the beam) related to the projection of the (generally 3D) field of the local refractive index increment Δn:

$$\Delta\phi = \frac{2\pi}{\lambda}\int \Delta n\ \mathrm{d}l \tag{1}$$

where the integral is taken along the optical path in the gas (here parallel to the substrate, disregarding any possible refraction). This integral represents the increment of the optical path length. As $\Delta n \sim \chi$ (where χ is the HFE-7100 vapor molar fraction in the gas, cf. Table 2),[24] the spatial nonuniformity of the phase is representative of the vapor cloud distribution. A possible thermal contribution into Δn due to evaporative cooling, estimated to be below 10%,[11] is disregarded. Indeed, the cooling is here of the order of 3 or 4 °C, as shown in simulations later on. This is about thrice lower than elsewhere,[11] while the HFE volatility (and thus the vapor concentration) is here about twice lower, hence the mentioned estimation. The wrapped-phase image, as in Figure 1, actually represents the $\Delta\phi$ field modulo 2π. The absolute value of the $\Delta\phi$ field can be obtained therefrom by unwrapping. Then, assuming the axial symmetry in conformity with the ARLES configuration, a tomographic reconstruction can in principle be performed so as to obtain the Δn (and, hence, χ) field. This can be accomplished by means of the inverse Abel transform (as realized e.g. elsewhere[11]), eq 1 then playing the role of a forward Abel transform. However, this is generally not feasible here, for the extent of the vapor cloud may well exceed the field of view (determined by the window size).[28] Fortunately though, the shape of the fringes in the wrapped-phase image is often representative of the iso-concentration lines. Therefore, the shape of the vapor cloud can well be judged qualitatively by the fringe pattern. Furthermore, the simulation results, considered later on in the present paper, can also be readily rendered in such a fringe-pattern form to facilitate the comparison.

FIRST RESULTS AND DISCUSSION

As a reference, the typical results of a ground experiment are represented in Figure 2a. We note that the vapor cloud clearly deviates from the spherical-cap isocontours that one would expect if only diffusion governed the dynamics of the vapor cloud. Indeed, the fully developed vapor cloud displays almost horizontal isocontours of the phase. While these isocontours do not correspond quantitatively to isoconcentration levels of vapor, it is nevertheless clear that these should also exhibit a strong flattening. Such flattening can be explained by a radially outward flow (gravity current), which is also an anticipated effect natural convection would have on such a heavy vapor cloud (e.g., Kelly-Zion et al.[29]). Indeed, the Grashof number turns out to be as large as 800 in the present case (cf. Supporting Information). A similar flow is after all observed in everyday (lab) life when opening a bottle of liquid nitrogen for instance and observing the cold air spreading over the floor.

So, what will happen when we remove gravity from the equation? This is essentially why the ARLES experiment was performed. In Figure 2b, the typical vapor cloud in microgravity is shown. A clear vertical stretching of the fringe contours is visible. This is the opposite to what was seen on ground (cf. Figure 2a). However, how can such a vertical stretching be explained? A radially inward flow at the base with an upward flow along the central axis must somehow be present in the vapor. As the surrounding nitrogen atmosphere is completely stagnant and passive, any motion has to be induced by the droplet itself. As it turns out, a liquid flow along the interface, from the contact line to the center, is well-known in literature.[23,30−32] These flows originate from temperature differences along the interface induced by evaporative cooling

https://doi.org/10.1021/acs.langmuir.3c00689
Langmuir XXXX, XXX, XXX−XXX

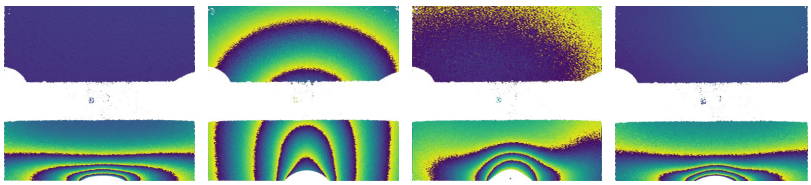

Figure 2. (a−d) Typical vapor cloud shapes, in terms of the phase-field images modulo 2π (wrapped-phase, fringe patterns), obtained in 1g and 0g experiments without and with an electric field. The wrapped-phase representation has been colored for better visualization.

and are of a thermal Marangoni nature. As heat supply toward the apex of the drop through the liquid is less effective than at the contact line, the temperature decreases from the contact line toward the apex (except maybe for poorly conducting substrates[32]). Therefore, along the interface, the thermal Marangoni flow pulls the liquid toward the symmetry axis, which can obviously entrain a gas flow in the same direction. It is such a "Marangoni jet" in the gas that is deemed to be captured in microgravity by vapor interferometry in Figure 2b. The Marangoni flow and jet must be sufficiently strong (the gas Peclet number must be larger than unity) to be visualizable by the fringes in this way. We further conjecture that for ground conditions, no such Marangoni jet is observable (cf. Figure 2a) due to an overwhelming flattening buoyancy action in view of the heavy vapor. In contrast, for a similar pendant droplet in normal gravity, the Marangoni jet is indistinguishable within a strong buoyancy vapor plume,[11] which only underscores the uniqueness of the present microgravity observation.

While it has demonstrated that the vapor cloud in microgravity conditions can be shaped by effects overlooked on Earth, these Marangoni flows are not easily manipulated and tunable in an arbitrary way as the effect is inherent to the droplet itself. This is why other exterior forces potentially capable of influencing the vapor cloud and evaporation rates were investigated in a microgravity environment, when they are not overwhelmed by buoyancy. Namely, as already stipulated earlier in this paper, we studied the effects of an electric field (EF) created by imposing a voltage between the annular-ring electrode and the substrate. An established vapor cloud in microgravity in the presence of EF is shown in Figure 2c, where a drastic change as compared to the case without EF (Figure 2b) can be observed. Even if this is a measurement in microgravity, the fringe pattern resembles more the one due to buoyancy under normal gravity (Figure 2a). Thus, it becomes clear that EF is capable of inducing a bulk movement in the vapor on its own, which is generally directed radially outward as the one due to buoyancy, although it here appears to be rather directed toward the outer rim of the electrode and not along the substrate. Let us underscore that this "electroconvection" clearly appears to be a bulk effect in the gas itself, not specifically related to any electric effect in the droplet (such as e.g. droplet shape deformation by EF). We had to go to microgravity to "discover" it, for it is not easily discernible under normal gravity as illustrated by Figure 2d, which on first glance does not appear too different from the corresponding fringe patterns in the absence of EF in Figure 2a. Yet, even under normal gravity, we can notice a subtle difference: the upper fringes turn upward near the edges in the presence of EF (vapor attraction to the outer rim of the electrode) instead of downward in the absence thereof. In Figure 2c, notice a slight asymmetry in the vapor field, which is presumably due to a somewhat eccentric placement of the electrode.

The most plausible reason behind the electroconvection in the gas is deemed to be dielectrophoresis, due to gradients of the dielectric permittivity of the gas ϵ_g caused by the vapor cloud. It is actually quite surprising such an effect would play any role at all given that ϵ_g is normally very close to unity for gases. For instance, $\epsilon_g \sim 1.0006$ for N_2. Yet an estimation carried out in Table 2 reveals a deviation of ϵ_g from unity well more pronounced for the HFE vapor (viz. $\epsilon_g \sim 1.015$ at its saturation molar fraction), which is partly explained by its large molecules and which inspires further confidence in the present conjecture.

To substantiate the conjectures put forth here as well as to gain a further physical insight, simulations have been carried out as described in the following sections.

MODEL

Simulations of an evaporating sessile droplet in the ARLES main evaporation cell are carried out in a 2D axisymmetric framework with the help of COMSOL Multiphysics software. We note that axial symmetry holds indeed to a large extent in the present setup. As per the parameters of the ARLES experiment, the droplet is here always an HFE-7100 one with a pinned contact line (contact radius R_c = 2 mm unless specified otherwise). It evaporates into pure nitrogen at a pressure p_{amb} = 105100 Pa. The substrate is maintained at a constant temperature T_{sub} = 28 °C. This is deemed to be a good assumption in view of a highly thermally conductive substrate (silicon wafer) in conjunction with a thermal controller maintaining the temperature at 28 °C. The measured substrate temperature deviations do not exceed 0.25 °C for both the ground and flight runs.[18] The material properties used in the analysis are defined at this temperature and pressure (where relevant) and listed in Table 2. It is only the surface tension and the saturation pressure (and consequently the saturation molar fraction of the vapor) that are treated as functions of temperature. As stipulated by the ARLES runs listed in Table 1, the levels of the gravity acceleration $\boldsymbol{g}$ considered are $\boldsymbol{g} = 0$ (approximating microgravity in the sounding-rocket runs) and $|\boldsymbol{g}| = 9.81\ m/s^2$ with $\boldsymbol{g}$ directed downward orthogonally to the substrate (as for the 1g runs in the ARLES ground test campaign). The electric field levels considered in the simulations are those used in the experiment: U = 0 (no electric field), 5.7, and 8 kV (cf. Table 1).

In the absolute majority of the present simulations, a droplet in the form of a spherical cap pinned at $r = R_c$ = 2 mm is assumed:

$$h(r) = \sqrt{\frac{R_c^2}{\sin^2\theta} - r^2} - \frac{R_c}{\tan\theta},\quad V = \frac{1}{3}\pi R_c^3(2+\cos\theta)\frac{\sin\theta}{(1+\cos\theta)^2} \tag{2}$$

https://doi.org/10.1021/acs.langmuir.3c00689
Langmuir XXXX, XXX, XXX−XXX

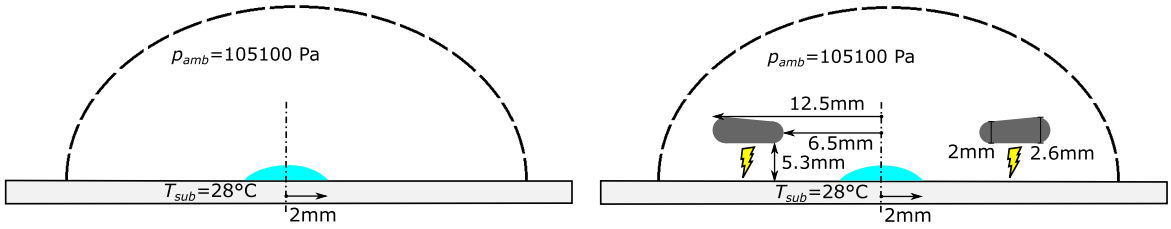

Figure 3. Configurations used in benchmark simulations. Apart from the "classical" one shown on the left (flat infinite substrate, no groove, gas filling half-space, asymptotic decay conditions at "infinity"), the only "extraneous" element it may involve is the ARLES annular-ring electrode as represented on the right.

for the local droplet height h as a function of the (cylindrical) radial coordinate r ($0 \le r \le R_c$) and for the droplet volume V, respectively. Here, θ is the contact angle (a function of V for the pinned spherical-cap droplet). The measured droplet shapes in microgravity without an electric field indeed turn out to be quite close to the spherical cap, whereas in normal gravity with or without an electric field, the distortion from the spherical cap is not judged drastic enough to warrant a special consideration beyond the spherical caps here (cf. the shapes outlined elsewhere[18]). However, there are two instances where such a spherical-cap approach is more problematic. First, it is the injection stage when, even if a spherical cap, the growing droplet is not immediately pinned at $r = R_c$. Nonetheless, for the sake of simplicity, it is here treated as immediately pinned. Second, in microgravity with an electric field the droplet shapes may be strongly distorted ("e-shapes", cf. Supporting Information). In such cases, a few test simulations are carried out with the e-shapes for comparison, whereas the majority of simulations are still accomplished using the spherical caps.

Herewith, two kinds of simulations are carried out:

(i) "Benchmark" quasi-steady simulations. The configuration used is the "classical" one, as shown in Figure 3, with formally an infinite flat substrate and the liquid occupying half-space. In this way, it is closer to the associated standard arrangements typically considered in the literature. The relevance to ARLES is well justified by the dimensions of the main evaporation cell being much larger than the droplet size, the latter being in turn much larger than the cross-section of the groove at which the droplet is pinned. The only "extraneous" element allowed in this classical configuration may be the presence of the ARLES annular-ring electrode, the benchmark simulations being accomplished both without and with the electrode for comparison (Figure 3, left and right, respectively). Two representative droplet volume values V = 2.9 and 5.8 μL (contact angles θ = 25.6° and 46.9°, respectively, for the pinned spherical-cap droplets), falling well into the experimental range (cf. Table 1), are chosen for the benchmark simulations here. Apart from providing ARLES-related reference points, the benchmark simulations are used for systematically analyzing the role of various physical factors on the vapor cloud and evaporation rate. For the cases in microgravity with an electric field, both spherical cap and e-shapes are simulated for comparison (in other cases only spherical-cap shapes are used). However, being essentially steady, the benchmark simulations are generally not suitable for the computation of the phase difference involved in eq 1, the reason being a generally insufficiently fast decay of χ at "infinity" for a reliable integral convergence. Therefore, to that purpose, one better rely upon "real-setup" simulations, which involve finite dimensions of the main evaporation cell (be them even large) and are besides transient (hence, an expected faster decay of χ anyway). Furthermore, they will permit the capture of the initial stages of droplet evaporation when the vapor cloud is not yet established.

(ii) Real-setup transient simulations. The real-setup transient simulations follow the course of the ARLES experiment as close as possible, the configuration being the axisymmetric/axisymmetrized one of the main evaporation cell shown in Figure 1. They are aimed at a detailed comparison with experiment in terms of the fringe patterns for the runs represented in Table 1. The droplet shapes are adopted in the form of the mentioned pinned spherical caps with the volume evolution $V(t)$ roughly approximated from experiment (cf. Supporting Information). This evolution consists of an injection stage up to the first (maximum) volume value shown in the fourth column of Table 1, followed by an evaporation stage down to the second (smaller) volume value. Borrowing $V(t)$ from experiment, rather than determining it from within the simulation itself, was here preferred in view of possible appreciable discrepancies between the measured and predicted evaporation rates (which is one of the discussion points throughout the present paper).

Note that the support legs of the electrode are always disregarded altogether within the axisymmetric approach used in the present paper, the electrode formally appearing as hanging in thin air axisymmetrically over the droplet (Figures 1 and 3).

We now proceed to a mathematical formulation of the problem of an evaporating sessile droplet in the context of the ARLES experiment.

A noteworthy feature of the present problem is that the gas density ρ_g cannot be assumed constant as it generally varies by the order of itself due to the vapor cloud generated by the evaporating droplet. Indeed, HFE-7100 is rather volatile (its molar fraction in the gas χ varying by the order of $\chi_{sat,0} \sim 0.3$) and possesses heavy molecules ($M_{HFE} \gg M_{N_2}$), see Table 2 for these and other properties. The effect of $\rho_g(\chi)$ is fully accounted for in the present model. However, we still remain in the usual framework of an incompressible flow, in the sense that ρ_g is not affected by hydrodynamic and hydrostatic pressure variations. The effect of a nonuniform temperature field, due to evaporative cooling, on ρ_g is also disregarded, as well as on all other gas and liquid properties, except for the surface tension and the saturation quantities, cf. Table 2. Indeed, evaporative cooling, $\Delta T \sim 3$ K, gives rise to the ρ_g variation on the order of $\Delta T/T \sim 1\%$ on account of the ideal gas laws and $T \sim T_{sub} \sim 300$ K, which is much smaller than the mentioned variation due to the presence of the vapor anyway. In contrast with ρ_g, the gas molar density n_g is here constant (under the latter two assumptions).

https://doi.org/10.1021/acs.langmuir.3c00689
Langmuir XXXX, XXX, XXX−XXX

Another noteworthy feature is accounting for the electric forces in the bulk of the gas phase (in those cases where the voltage is applied). Indeed, as discussed in First Results and Discussion, the experimental results obtained in microgravity clearly guide us to incorporate such forces into the model in spite of ϵ_g being close to unity for the gases. We note that, among the three bulk forces,[33] the electrostriction plays no role here as it can merely be absorbed into the pressure term to yield a redefined, hydrodynamic pressure $\hat{p}_g$ (marked by a hat). The Coulomb force is not present for there are no free electric charges in the gas bulk. However, there remains the dielectrophoretic force, explicitly included into the Navier–Stokes equations below. It is related to the gradients of ϵ_g on account of the vapor cloud, $\epsilon_g = \epsilon_g(\chi)$.

Thus, the continuity and Navier–Stokes equations in the gas ($\boldsymbol{v}_g$ being the gas velocity field) are written as

$$\partial_t \rho_g + \nabla\cdot(\rho_g \boldsymbol{v}_g) = 0 \tag{3}$$

$$\rho_g(\partial_t \boldsymbol{v}_g + \boldsymbol{v}_g\cdot\nabla\boldsymbol{v}_g) = -\nabla\hat{p}_g + \nabla\cdot\left(\mu_g\left(\nabla\boldsymbol{v}_g + \nabla\boldsymbol{v}_g^T - \frac{2}{3}\mathbf{I}\nabla\cdot\boldsymbol{v}_g\right)\right) - \frac{1}{2}\epsilon_0|\nabla\varphi|^2\nabla\epsilon_g + (\rho_g - n_g M_{N_2})\boldsymbol{g} \tag{4}$$

where ρ_g, ϵ_g, and the gas dynamic viscosity μ_g are all functions of χ (cf. Table 2 and Supporting Information). Here $\mathbf{I}$ is the unit tensor and φ is the field of the electric potential. In the cases when no voltage is applied, we have $\nabla\varphi = 0$ and hence the dielectrophoretic force, the last-but-one term in eq 4, vanishes. We note that no Boussinesq approximation is involved in eqs 3 and 4, the last term in eq 4 being modified by a constant $n_g M_{N_2}\boldsymbol{g}$ just for convenience.

Notwithstanding the presence of the gradient $\nabla\epsilon_g$ in eq 4, the small deviation of ϵ_g from unity is neglected within the problem for the electric field in the gas:

$$\nabla^2\varphi = 0 \tag{5}$$

$$\varphi = 0 \text{ at the droplet surface, substrate, walls,}\quad \varphi = U \text{ at the electrode} \tag{6}$$

so that φ is governed by merely the Laplace equation, cf. eq 5. The boundary conditions given by eq 6 imply electrically conducting boundaries. What is less obvious is that the droplet is herewith treated as electrically conducting too. The rationale behind using such a conducting-liquid assumption here is that it is found to lead to a better *a posteriori* verification of the force balance within an experimentally measured droplet shape in an electric field than a dielectric-liquid assumption (cf. Chapter 8 of ref 34, where also noted is an estimated relaxation time of only 5.7 ms, justifying the premise from the theoretical viewpoint). Note that both such limiting cases are contained within the Taylor-Melcher leaky dielectric model (the limits of small and large electrical relaxation times, respectively).[33,35] We also note that, within the assumptions made, the electric field decouples from the velocity and concentration fields (and is in this sense universal, just depending on the droplet shape). The typical electric field lines for the ARLES configuration have already been plotted elsewhere[18] (cf. Figure 2 therein).

The vapor molar fraction χ is governed by the advection-diffusion equation

$$\partial_t\chi + \left(\boldsymbol{v}_g + D_g\frac{M_{HFE} - M_{N_2}}{M_{HFE}\chi + M_{N_2}(1-\chi)}\nabla\chi\right)\cdot\nabla\chi = D_g\nabla^2\chi \tag{7}$$

where the advection is realized by means of a so-called molar-averaged velocity (the term in the parentheses on the left-hand side).[36] Such a form of the equation is useful when ρ_g is greatly variable, whereas the molar density n_g is constant (as assumed here).

The boundary conditions from the gas side include no slip and impermeability at solid surfaces (including the substrate not covered by the droplet):

$$\boldsymbol{v}_g = 0,\quad \partial_n\chi = 0 \text{ at solid surfaces} \tag{8}$$

On the other hand,

$$v_{g,n} = v_{\Sigma,n} + \frac{j}{\rho_g},\quad v_{g,\tau} = v_{l,\tau},\quad \chi = \chi_{sat}(T_l) \text{ at the droplet surface} \tag{9}$$

where

$$j = -\frac{n_g M_{HFE} D_g}{1-\chi}\partial_n\chi \text{ at the droplet surface} \tag{10}$$

is the evaporation flux density (kg/m^2 s), the subscripts "n" and "τ" denote the normal and tangential components, respectively, the normal points to the gas, $v_{\Sigma,n}$ is the normal velocity of the surface itself (owing to the droplet volume change during the injection and evaporation), $\boldsymbol{v}_l$ is the velocity field in the liquid. According to eq 9, the normal velocity of the gas is due to $v_{\Sigma,n}$ and the evaporation, the tangential velocity is continuous across the gas–liquid interface (no slip), and the molar fraction is given by its saturation value at the local liquid temperature T_l (local phase equilibrium). With eq 10, the (integral) evaporation rate of the droplet J (kg/s) is obtained by integrating over the droplet surface area:

$$J = \int\int j\ \mathrm{d}A \tag{11}$$

Note that to express J in μL/s (as often used here), one should multiply J in kg/s by $10^9/\rho_l$ (where ρ_l is the liquid density, cf. once again Table 2). We shall also widely use a dimensionless version of the evaporation rate

$$J^* \equiv \frac{J}{D_g\rho_{sat,0}R_c} \tag{12}$$

(as we already did in Table 1).

Once again referring to the experimental results obtained in microgravity (First Results and Discussion), this time those obtained in the absence of the electric field, we note that they clearly point to the importance of the Marangoni convection in the droplet for the vapor cloud shape. Furthermore, another consequence of evaporative cooling is the reduction of the saturation pressure along the droplet surface. Thus, even if we are mainly interested in the vapor cloud, consideration of the velocity $\boldsymbol{v}_l$ and temperature T_l fields in the liquid phase cannot be excluded from the model. Their impact on the vapor cloud is actually already anticipated in the boundary conditions given by eq 9. We use a standard incompressible formulation:

$$\nabla\cdot\boldsymbol{v}_l = 0 \tag{13}$$

$$\rho_l(\partial_t\boldsymbol{v}_l + \boldsymbol{v}_l\cdot\nabla\boldsymbol{v}_l) = -\nabla\hat{p}_l + \mu_l\nabla^2\boldsymbol{v}_l \tag{14}$$

$$\rho_l c_{p,l}(\partial_t T_l + \boldsymbol{v}_l\cdot\nabla T_l) = \lambda_l\nabla^2 T_l \tag{15}$$

with the boundary conditions

https://doi.org/10.1021/acs.langmuir.3c00689
Langmuir XXXX, XXX, XXX−XXX

$$v_{l,n} = 0,\ \mu_l \boldsymbol{n}\cdot(\nabla \boldsymbol{v}_l + \nabla \boldsymbol{v}_l^T)\cdot\boldsymbol{\tau} = -\gamma_T \partial_\tau T_l,$$
$$\lambda_l \partial_n T_l = -\mathcal{L} j \ \text{at the droplet surface} \quad (16)$$

where $\boldsymbol{n}$ and $\boldsymbol{\tau}$ are the normal and tangential unit vectors, and

$$\boldsymbol{v}_l = 0, \quad T_l = T_{\text{sub}} \ \text{at the substrate} \quad (17)$$

(underneath the droplet). The following assumptions/simplifications have been made. The evaporative flow in the droplet and the buoyancy convection (in the 1g case) are disregarded against the Marangoni convection, hence the first condition in eq 16 and no buoyancy term in eq 14, respectively. The dynamic viscosity and thermal conductivity of the gas are neglected against those of the liquid in the second and third conditions given by eq 16, involving the Marangoni (thermocapillary) stresses and evaporative cooling, respectively. For the new material properties introduced, we refer to Table 2 as usual.

This completes the problem formulation in principle. Some further nuances that may still need to be clarified as far as the real-setup (transient) simulations are concerned can be found in Supporting Information (cf. the section on droplet volume evolution therein). For the benchmark (quasi-steady) simulations, we additionally need to specify $\partial_t = 0$ throughout, i.e., in eqs 3, 4, 7, 14, and 15, as well as $v_{\Sigma,n} = 0$ in eq 9.

At last, for comparison and for the sake of appreciating the role of each physical effect, supplementary benchmark simulations are also realized in a fully isothermal formulation, without evaporative cooling and the Marangoni effect. In this case, the part of the formulation concerning the liquid phase is totally discarded, while the second and third boundary conditions in eq 9 are merely replaced with $v_{g,\tau} = 0$ and $\chi = \chi_{\text{sat},0}$, respectively. We also test a "halfway" approach toward such a fully isothermal formulation in order to discriminate between the two impacts of evaporative cooling (the Marangoni effect and the T-dependence of χ_{sat}). Namely, we switch off just the T-dependence in χ_{sat}, while still keeping in place the liquid-phase consideration, the Marangoni effect and evaporative cooling. In this case, it is only the last boundary condition in eq 9 that is replaced with $\chi = \chi_{\text{sat},0}$, the remainder of the benchmark formulation unchanged.

FURTHER RESULTS AND DISCUSSION

Benchmark Quasi-Steady Results. We start with the discussion of the benchmark computation results, which are provided in Tables 3 and 4 and Figures 4−6. They are, to a high degree, self-explanatory, and several lines of conclusions can be drawn therefrom. We shall here dwell upon the following ones.

First, the presence of the electrode merely gives rise to a minor ($\lesssim$2%) reduction of the evaporation rate (cases a, b, k, l vs d, e, n, o, respectively, in Table 3, and a, b, h, i vs c, d, j, k, respectively, in Table 4), even if the streamlines far away from the droplet may obviously be affected by the electrode as it is a flow obstacle (cf. Figure 4).

Second, focusing on fully isothermal simulations (no Marangoni, in particular) in the absence of external forces (i.e., 0g and $U = 0$) and in the absence of the electrode, which are represented by cases b in Tables 3 and 4, we notice that the evaporation rates are ∼20% higher than in the corresponding pure-diffusion numbers (mentioned in the footnotes of Tables 3 and 4). This is an expected result given the presence of Stefan flow in the present simulations and its absence in pure-diffusion ones. Recall here the denominator in eq 10, which is different from merely unity just on account of Stefan flow. Such an outward Stefan flow can be appreciated in Figure 4a (although with an electrode obstacle in this case). Regardless of the flow, just as in the pure-diffusion case, there is always an integrable singularity of the evaporation flux density j^* at the contact line ($r \to R_c$), cf. Figure 6.

Third, still staying in 0g and at $U = 0$, but now within the full formulation (with evaporative cooling and thermal Marangoni effect), we notice that the corresponding conjecture drawn in First Results and Discussion is obviously confirmed by the simulations. There is indeed a Marangoni convection/recirculation inside the droplet, toward the (colder) apex along the surface (cf. Figure 5), which is here strong enough to engage a visible vapor jet in the gas. The Marangoni recirculation is understandably stronger for a larger droplet: compare Figure 4b,c and the corresponding $v_{\Sigma,\tau}$ curves in

Table 3. Benchmark Quasi-Steady Simulation Results for a Droplet of $V = 2.9\ \mu$L

case	g	*Ma*	$\chi_{\text{sat}}(T)$	drop shape	electrode	U (kV)	J^*
(a)	0g	yes	yes	sph. cap	none	n/a	5.0
(b)	0g	no	no	sph. cap	none	n/a	5.2[a]
(c)	0g	yes	no	sph. cap	none	n/a	5.6
(d)	0g	yes	yes	sph. cap	yes	0	4.9
(e)	0g	no	no	sph. cap	yes	0	5.1
(f)	0g	yes	yes	sph. cap	yes	5.7	6.5
(g)	0g	yes	yes	sph. cap	yes	8	6.8
(h)	0g	yes	yes	e-shape[c]	yes	8	6.6[b]
(i)	0g	no	no	sph. cap	yes	8	7.5
(j)	0g	no	no	e-shape[c]	yes	8	7.2
(k)	1g	yes	yes	sph. cap	none	n/a	8.5
(l)	1g	no	no	sph. cap	none	n/a	10.1[d]
(m)	1g	yes	no	sph. cap	none	n/a	9.6
(n)	1g	yes	yes	sph. cap	yes	0	8.4[b]
(o)	1g	no	no	sph. cap	yes	0	9.9
(p)	1g	yes	yes	sph. cap	yes	8	8.3[b]
(r)	1g	no	no	sph. cap	yes	8	9.5

[a]Cf. 4.34 for pure diffusion[13] (see Supporting Information). [b]Used in Table 1. [c]See Supporting Information. [d]Cf. 10.0 from correlation[29] (see Supporting Information).

Table 4. Benchmark Quasi-Steady Simulation Results for a Droplet of $V = 5.8\ \mu$L

case	g	*Ma*	$\chi_{\text{sat}}(T)$	drop shape	electrode	U (kV)	J^*
(a)	0g	yes	yes	sph. cap	none	n/a	6.0
(b)	0g	no	no	sph. cap	none	n/a	5.6[a]
(c)	0g	yes	yes	sph. cap	yes	0	5.9[b]
(d)	0g	no	no	sph. cap	yes	0	5.5
(e)	0g	yes	yes	sph. cap	yes	5.7	7.3
(f)	0g	no	no	sph. cap	yes	5.7	7.9
(g)	0g	yes	yes	e-shape[c]	yes	5.7	7.4[b]
(h)	1g	yes	yes	sph. cap	none	n/a	9.6
(i)	1g	no	no	sph. cap	none	n/a	12.4[d]
(j)	1g	yes	yes	sph. cap	yes	0	9.5
(k)	1g	no	no	sph. cap	yes	0	12.2
(l)	1g	yes	yes	sph. cap	yes	5.7	8.9
(m)	1g	no	no	sph. cap	yes	5.7	10.6

[a]Cf. 4.75 for pure diffusion[13] (see Supporting Information). [b]Used in Table 1. [c]See Supporting Information. [d]Cf. 10.9 from correlation[29] (see Supporting Information).

https://doi.org/10.1021/acs.langmuir.3c00689
Langmuir XXXX, XXX, XXX−XXX

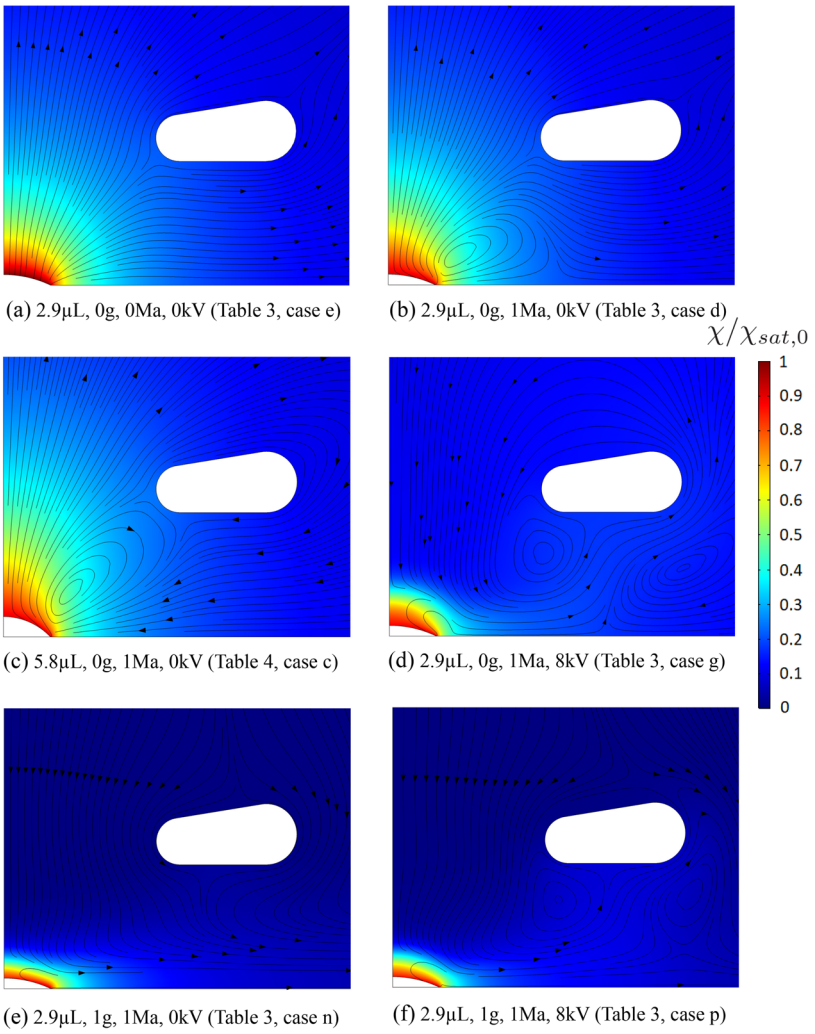

Figure 4. (a–f) Benchmark quasi-steady simulation results in the indicated cases for the vapor concentration field (color bar normalized to the saturation concentration at the ambient temperature) and the streamlines in the gas phase ("uniform density" plotting by Comsol 5.4).

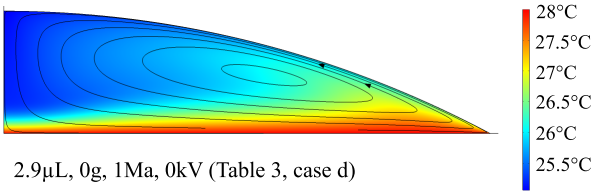

Figure 5. Benchmark quasi-steady simulation results: example of the temperature field and Marangoni recirculation inside the droplet.

Figure 6. The Marangoni jet in the gas in Figure 4c is especially noticeable by contrast with the isothermal case of Figure 4a, which signals that the gas Peclet number $Pe = R_c u/D_g$ must be significantly larger than unity. Indeed, it turns out to be of the order of 7, if we use for the velocity scale u the maximum velocity values appearing in Figure 6 (cf. Table 2 for R_c and D_g). A recirculation zone in the gas is attributed to the Marangoni jet developing on the background of a still outward Stefan flow and its existence is not related to the presence of the electrode.

One would expect such Marangoni convection to give rise to higher evaporation rates as compared to the case in the absence thereof. Indeed, this turns out to be true for a larger droplet (cf. cases a and c versus b and d, respectively, in Table 4). However, this is not so for a smaller droplet (cf. cases a and d versus b and e, respectively, in Table 3), when the Marangoni velocity is weaker. The reason is clarified by an artificial halfway case c of Table 3, where evaporative cooling is accounted for as the basic cause for Marangoni convection, but disregarded in the saturation conditions at the droplet surface. In this way, we see that Marangoni convection as such does lead to an evaporation rate increase. However, it is just a smaller vapor pressure at the cooler parts of the surface that can inverse the overall trend.

Fourth, simulations in 0g but in the presence of an electric field ($U \neq 0$) do confirm an appreciable elecroconvection in the gas, conforming to the conjecture made in First Results and Discussion from the interferograms of the sounding-rocket experiments. As one can observe by comparing Figure 4d,e, the action of the electric forces (in 0g) bears resemblance to that of the buoyancy (in 1g at $U = 0$) in the sense that either of the forces flattens the vapor cloud above the droplet and overturns the Marangoni jet outward horizontally. Herewith, the main action of the electric force seems to be directed toward the outer rim of the electrode (and it is along this pathway that one observes an unusual curling of the fringes in Figure 2c). In both these cases, the additional forcing gives rise to an evaporation rate increase (cf. cases d versus f, g, n in Table 3,

https://doi.org/10.1021/acs.langmuir.3c00689
Langmuir XXXX, XXX, XXX−XXX

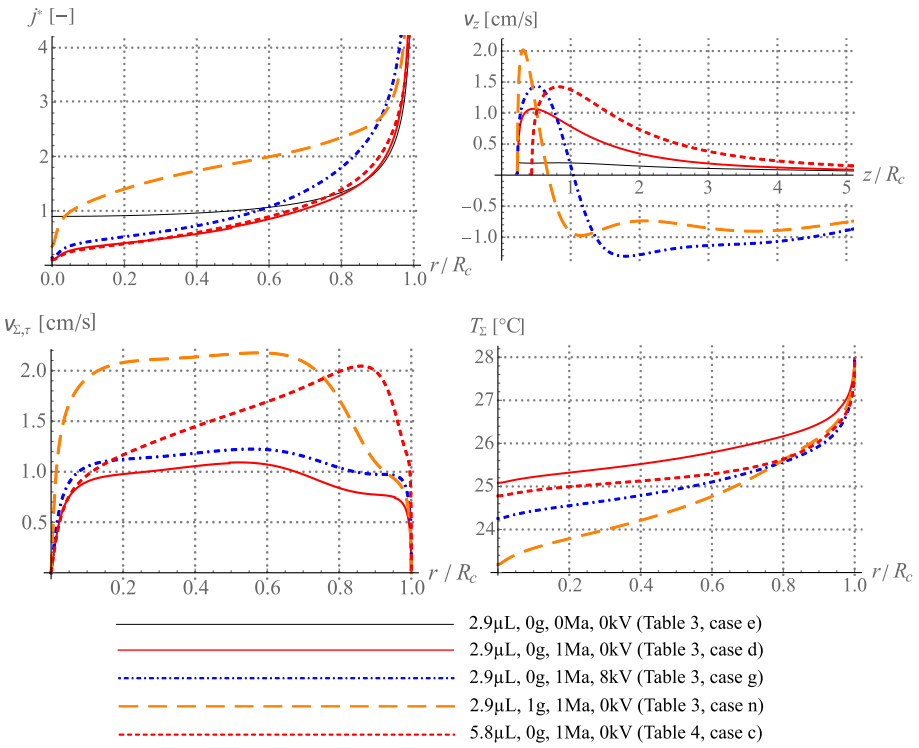

Figure 6. Benchmark quasi-steady simulation results: distributions of the dimensionless evaporation flux density j^* (j normalized to the scale $D_g \rho_{sat,0}/R_c$, always an integrable singularity toward the contact line), vertical velocity v_z in the gas along the symmetry axis (positive when away from the substrate), tangential velocity at the surface $v_{\Sigma,\tau}$ (here defined positive when toward the apex) and surface temperature T_Σ in the indicated cases.

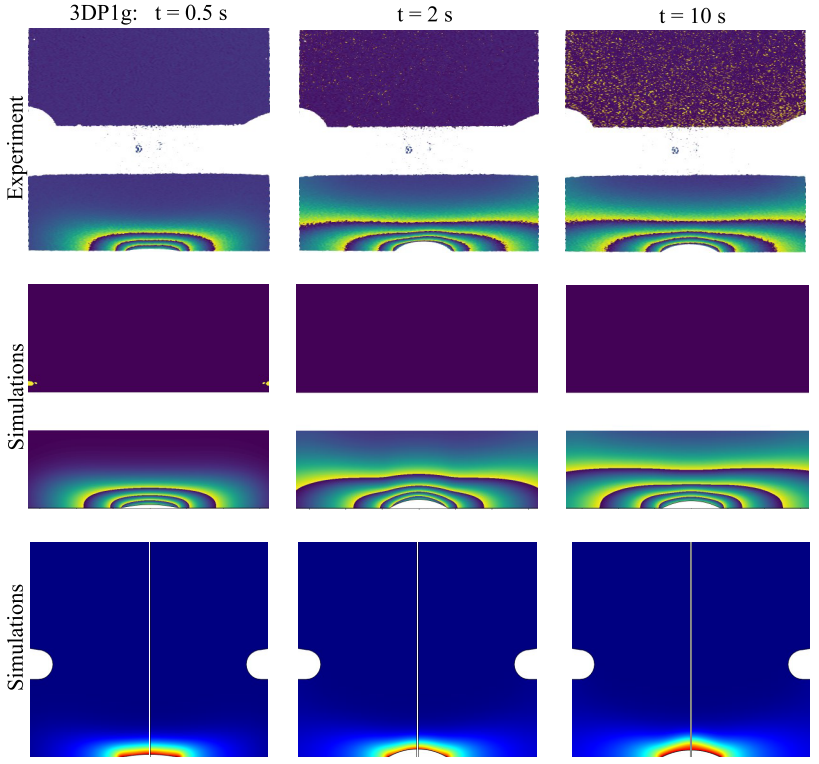

Figure 7. Experiment and real-setup transient simulations for a ground run (1g) with no electric field. For each simulated fringe pattern, the associated vapor concentration field appears right below (with the color bar the same as in Figure 4). The following few figures are organized in the same way.

and c versus e and j in Table 4). Furthermore, were it not for evaporative cooling and the Marangoni convection in their way, either of these forcing factors would have ensured even greater evaporation rates (cf. cases i and l in Table 3, and f and k in Table 4). On the other hand, the Marangoni convection is not a constant and is actually increased by the forcing factors

https://doi.org/10.1021/acs.langmuir.3c00689
Langmuir XXXX, XXX, XXX−XXX

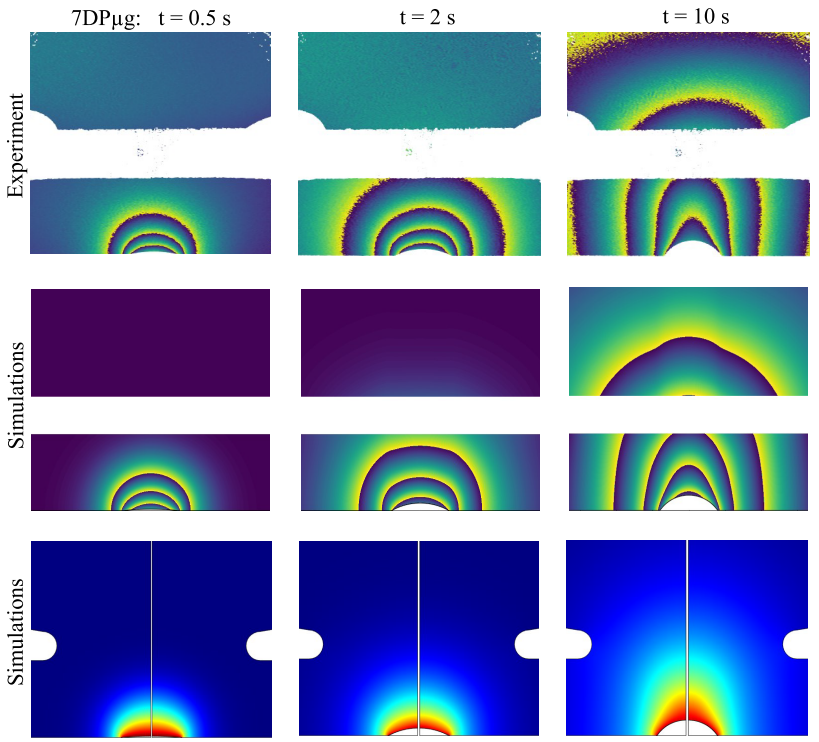

Figure 8. Experiment and real-setup transient simulations for a sounding-rocket run (0g) with no electric field.

(cf. the $v_{\Sigma,\tau}$ curves in Figure 6): this is no surprise given that the evaporation rate, evaporative cooling and Marangoni convection are all coupled processes.

Fifth, a combination of the two forcing factors (electric field and buoyancy) nonetheless does not appear to be efficient with respect to a possible further increase of the evaporation rate: in fact, switching on the electric field ($U \neq 0$) in normal gravity (1g) can be seen to bring to somewhat lower evaporation rates (cf. cases n versus p in Table 3, and j vs l in Table 4). Furthermore, such a combination gives rise to a complex system of vortexes (Figure 4f), worth a separate study.

Sixth, concerning the simulations in 0g in the presence of an electric field ($U \neq 0$), we note that using the spherical-cap shapes gives rise to roughly the same evaporation rates as for the e-shapes under otherwise equal circumstances (cf. cases g versus h in Table 3, and e versus g in Table 4).

Seventh, the representative evaporation rates obtained in the benchmark simulations are shown in a separate column of Table 1. We can state that in 1g the agreement with the corresponding values measured in experiment is rather satisfactory. In contrast, we see that the values measured in 0g turn out to be overpredicted by some 50%. Possible reasons for such a discrepancy are further investigated later on. However, the finding that switching on the electric field increases the evaporation rates in 0g is consistent between the experiments and simulations.

Comparison of Experimental and Simulated Fringe Patterns. A first appreciation of the experimental results in terms of the fringe patterns was already provided in First Results and Discussion, which permitted us to conjecture a picture of the phenomenon and guide us through the model construction in Model. Further details, now together with the corresponding simulation results, are represented in Figures 7−10 for ground (1g) and sounding-rocket (0g) runs without or with an electric field. A sequence of phase-field images

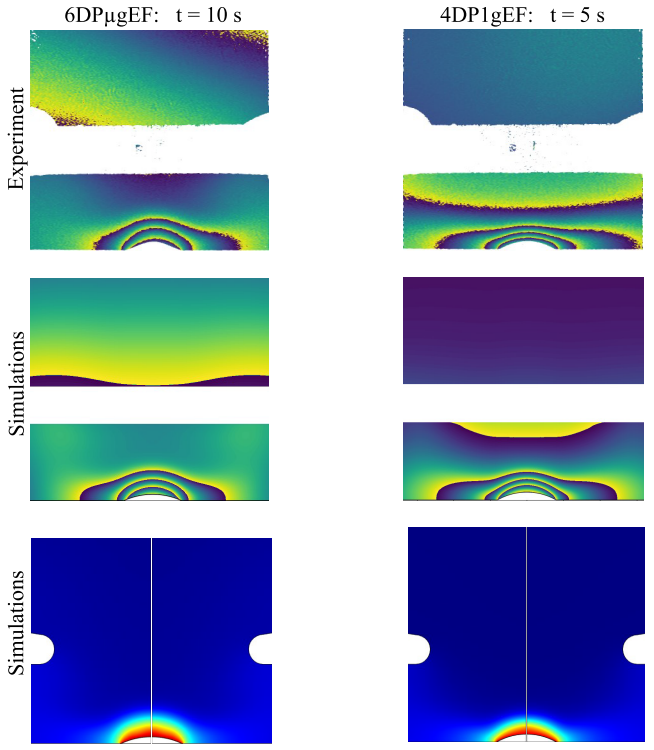

Figure 9. Experiment and real-setup transient simulations for runs with an electric field (U = 8 kV). Left: sounding rocket (0g). Right: normal gravity (1g).

(modulo 2π) is shown displaying the progression of the vapor cloud. The reader is also referred to full experiment and numerical simulation Movies S1−S10 of the fringe pattern evolution for each run shown in Figures 7−10. Between t = 0.5 s and t = 2 s, injection of the liquid continues, leading to an

https://doi.org/10.1021/acs.langmuir.3c00689
Langmuir XXXX, XXX, XXX−XXX

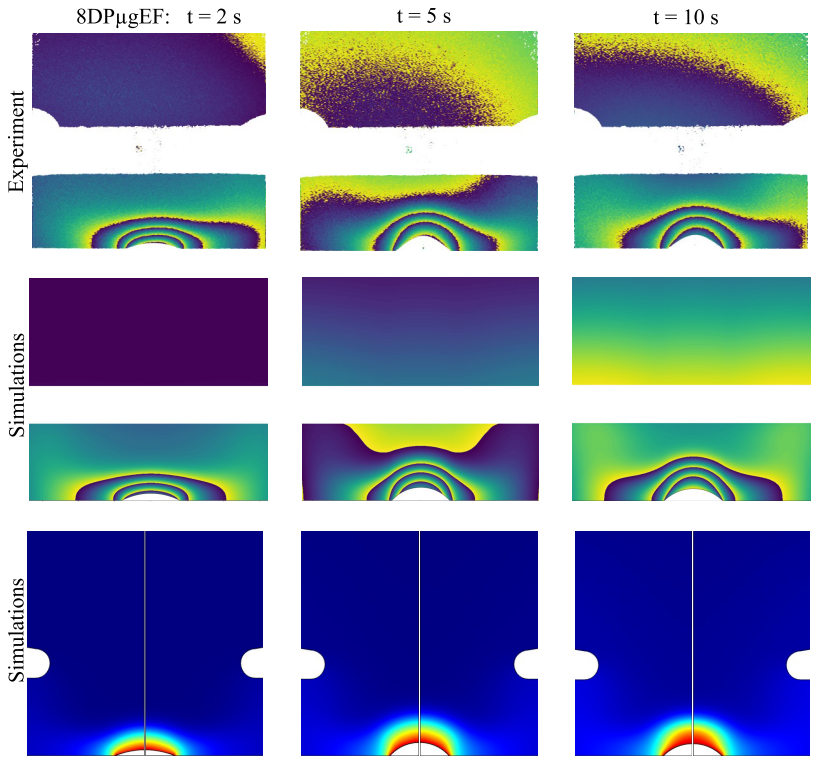

Figure 10. Experiment and real-setup transient simulations for a sounding-rocket run (0g) with an electric field (U = 5.7 kV).

increasing volume. Between t = 2 s and t = 10 s, evaporation leads to a slight reduction of the droplet volume. Note that the vapor cloud is already quite extensive in the first image (taken 0.5 s after the start of the injection as in Figures 7 and 8). The vapor cloud flattening typical for 1g is observed from the very beginning (Figure 7). In contrast, the Marangoni jet typical for 0g gets sufficiently developed only after an initial, injection stage corresponding to the first two instances, during which the vapor cloud distinctly displays a spherical-shell-like pattern typical for pure diffusion (cf. Figure 8). It has indeed been demonstrated that during this initial stage the Marangoni flow is weakened, due to the thermal supply of the injected fluid.[37] We also note that for the run 6DPμgEF (but not the other runs with an electric field) the droplet is initially strongly perturbed by Taylor-cone formation, whereas Figure 9 (left) for this run already corresponds to an established, calm regime. Peculiar vapor-interferometric patterns in the presence of the Taylor cone for 6DPμgEF can be observed in the experiment Movie S9 (although not in the simulations, which are here *a priori* based on a spherical-cap shape).

Overall, the agreement between the experiment and simulations appears to be fairly good, which basically further validates the conjectures already advanced in First Results and Discussion and an additional insight gained in the previous subsection. Furthermore, the original axisymmetric vapor concentration fields obtained in the simulations are also provided in Figures 7−10 underneath the associated fringe patterns to which they give rise by means of eq 1 taken modulo 2π. One can notice that even if, as already mentioned, the fringes do not coincide one-on-one with the iso-concentration lines, their shapes resemble rather much qualitatively. Thus, one gets a correct idea of the vapor cloud shape directly from the fringe patterns. Notice also that the vapor cloud shapes earlier discussed in relation to the benchmark quasi-steady simulations (Figure 4) represent well the typical ones obtained in the real-setup transient simulations (Figures 7−10), as expected.

Interferometric Phase and Inquiry into Malfunctions. A good agreement between experiment and theory in terms of the fringe patterns makes us once again wonder why the measured evaporation rates in 0g (but not in 1g) turn out to be significantly lower than the computed ones, cf. Table 1. After all, similar vapor clouds are expected to correspond to similar evaporation rates.

This point is further explored in Figure 11, where we examine the phase evolution at certain selected points in the field of view of the camera. So far, we have been using the wrapped (i.e., modulo 2π) phase in all representations, which was actually quite handy in view of a convenient visualization in terms of the fringes. However, now in Figure 11, we use the true, absolute values of the phase $\Delta\phi$. For the experimental results, these come from an unwrapping procedure applied to the primarily obtained, wrapped phase. For the (real-setup) simulations, these are in fact already a primary result computed from eq 1 (after which we had to apply a modulo 2π to recover the fringe representation).

For comparison, we have also included a simulation at an HFE-7100 ambient relative humidity (RH) of 30% (whereas RH = 0% in all other simulations of the present paper), which would roughly reconcile the computed and measured 0g evaporation rates in Table 1. (We note that for the simulations at finite RH, the input of Table 2 is modified to $\Delta n(\chi) = 0.00147(\chi - \chi_{sat,0}\,\mathrm{RH}/100)$, which is used in eq 1.) The issue is that one of the hypotheses advanced by the ARLES Science Team during discussions was a nonideal flushing of the evaporation cell between the runs occurring in 0g, leaving behind a considerable residual HFE-7100 humidity in the gas and hence giving rise to lower evaporation rates (cf. also

https://doi.org/10.1021/acs.langmuir.3c00689
Langmuir XXXX, XXX, XXX−XXX

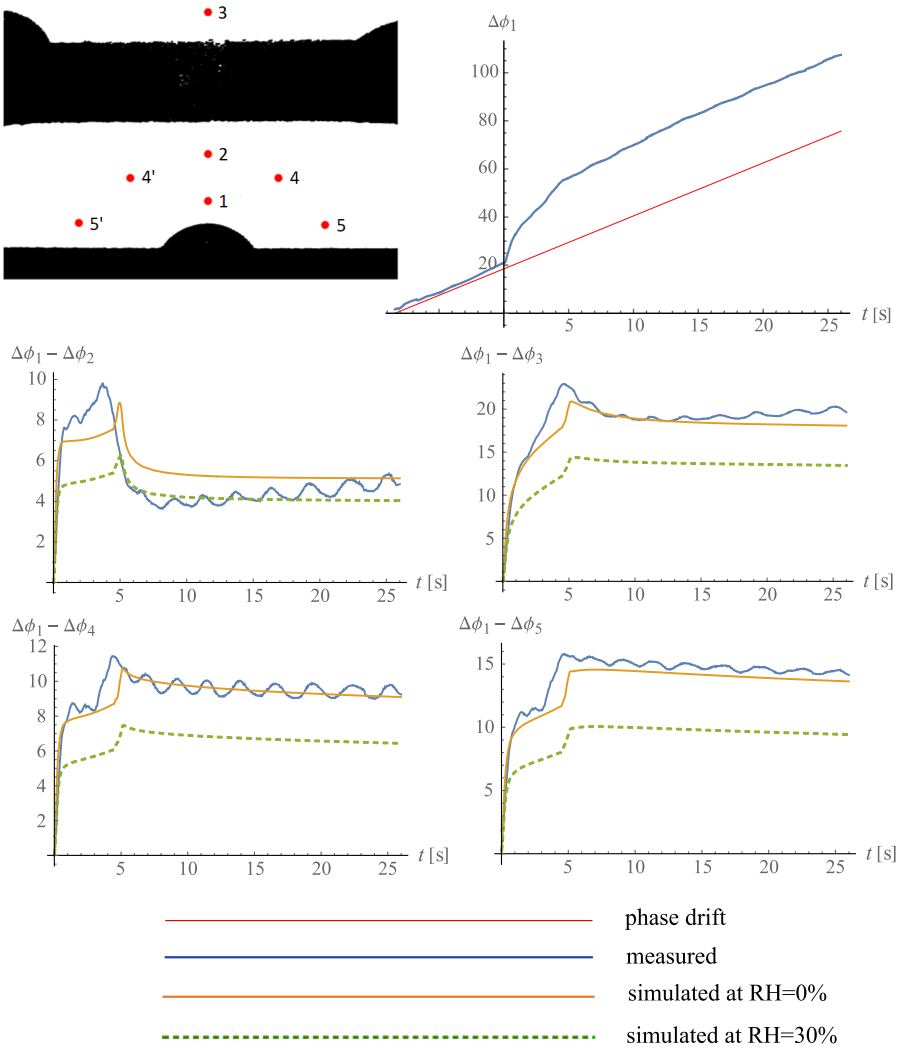

Figure 11. (Unwrapped) phase evolution $\Delta\phi(t)$ for the droplet 7DPμg at/between the shown selected points: 1) $\{x, z\} = \{0, 2\}$ mm, 2) $\{x, z\} = \{0, 4\}$ mm, 3) $\{x, z\} = \{0, 10\}$ mm, 4) $\{x, z\} = \{3, 3\}$ mm, 5) $\{x, z\} = \{5, 1\}$ mm. Subscripts correspond to point numbers. For the positions beyond the symmetry line (points 4 and 5), the measured phase shown is symmetrized (by taking the average with the corresponding symmetric points 4′ and 5′).

Supporting Information). Now, from Figure 11, we see that this hypothesis is not supported by our analysis, for the simulations for RH = 0% correspond incomparably better to experiment than those for RH = 30%.

Therefore, another possible hypothesis, that of leaking into the droplet from a very considerable "dead volume" of the liquid in the injection system that remains in a permanent contact with the droplet in the present setup, is deemed to be a more plausible one. If such leakage exits, it will obviously distort the $V(t)$-based side-view evaporation rate measurements. However, even if not unimaginable in such circumstances, the precise cause of such leakage and the reason why it would occur only during the sounding-rocket runs remain unestablished. At the same time, as already mentioned, the experimental results correctly capture an increase of the evaporation rate due to the presence of an electric field in 0g (cf. Table 1).

Figure 11 (cf. the second panel) also reveals a parasitic phase drift, uniform in space and apparently constant in time, not even related to the presence of a droplet and taking place well before the injection (i.e., for $t < 0$ in present conventions), where one would normally expect $\Delta\phi = 0$. It occurs only in the sounding-rocket (0g) runs and is not significant in the ground (1g) runs. A conjecture on its nature is advanced in Supporting Information. Here it just suffices to note that the experimental results presented in First Results and Discussion were actually based upon $\Delta\phi$ with an already subtracted phase drift (even if this was not absolutely necessary for the typical fringe patterns given that the fringes are representative of the gradient of the phase field while the drift is uniform). In the context of the present subsection, we get rid of the drift issue by considering the difference of $\Delta\phi$ between the various points, as shown in the last four panels of Figure 11.

CONCLUSIONS

Vapor interferometry has once again shown itself as an effective tool in analyzing the physics of an evaporating droplet. It helped to make the most of an exclusive opportunity offered by the microgravity (sounding rocket) experiment. A number of phenomena were revealed or visualized in a way not done before. The simulations have helped to substantiate the thereby made conjectures and to further quantify and analyze

https://doi.org/10.1021/acs.langmuir.3c00689
Langmuir XXXX, XXX, XXX−XXX

the results. Even when the inverse Abel transform to recover the vapor concentration field directly from experiment is not quite feasible (due to the vapor cloud extending beyond the field of view), the interferometric fringe patterns prove to be well representable of iso-concentration lines, permitting to judge upon the shape of the vapor cloud. All experiments and simulations were performed for the conditions of the ARLES sounding-rocket experiment: 28 °C, ambient nitrogen atmosphere at 1.051 bar, HFE-7100 as a working liquid, pinned sessile droplet with a contact radius of 2 mm.

In particular, going to microgravity permitted to reveal a Marangoni jet in the gas along the symmetry axis, which became apparent from a corresponding jet-like stretching of the fringes. It stems from and in this sense implicitly visualizes a strong Marangoni recirculation in the sessile droplet (order of magnitude of centimeters per second as disclosed by the simulations), directed from the contact line toward the apex along the surface. It is of a thermocapillary (thermal Marangoni) nature, while the temperature differences owe themselves to evaporative cooling. The computed differences between the contact line zone (hotter) and the apex (colder) are of the order of three or four degrees. If the Marangoni flow were not essential, the fringes would rather be of a roughly hemispherical shape (as for the pure-diffusion solution). Under normal gravity, the fringes are strongly flattened by buoyancy (heavy vapor) as typical for gravity currents over a flat substrate. Even if the simulations indicate that the Marangoni flow in the droplet is still strong (and even stronger) under normal gravity, it does not show up in the fringe pattern, which is totally dominated by buoyancy.

In the cases when the electric field was switched on, the situation in the microgravity experiment changed drastically. To our surprise, this was related to an effect in the gas phase itself (and not in the droplet), namely to dielectrophoresis due to gradients of the gas dielectric permittivity in the vapor cloud. It is apparently due to a large size of the HFE-7100 molecules that the small deviation of the gas dielectric permittivity from unity is here 2 orders of magnitude more pronounced than typically for gases (e.g., nitrogen), rendering the effect far from being negligible. From the viewpoint of the vapor cloud shape and induced flow, the dielectrophoretic effect acts quite similarly to buoyancy in the droplet vicinity, in particular overturning the Marangoni jet. However, at a larger scale, the vapor now appears attracted to the outer rim of the angular-ring electrode rather than flowing along the substrate like a gravity current. This is signaled by a corresponding deformation of the fringes toward the outer rim as well as observed in simulations. Once again, the microgravity environment much helped in disclosing the phenomenon in question. Under normal gravity, it is largely camouflaged by buoyancy, even though it can still be discerned with a close look at the fringes right below the electrode.

In general, a fairly good agreement between the measured and simulated fringe patterns is obtained in all cases, confirming our picture of the phenomena. Real-setup transient simulations were used to this purpose, even at larger times for already rather established vapor clouds, to avoid the issues of the vapor cloud decay far away from the droplet, to which the integral along the optical path may be quite sensitive (up to nonconvergence in steady cases with an asymptotically infinite domain). On the other hand, benchmark quasi-steady simulations have also been performed to systematically study the role of various physical factors on the vapor cloud shape and typical evaporation rates.

One can mention the following findings of the benchmark simulations. The presence of the annular-ring electrode in the way of the vapor only minimally affects the evaporation rates (reduction by ∼2%). Comparing the real droplet (with the thermal Marangoni flow and evaporative cooling) with an idealized isothermal droplet (without those effects), one can find out that the evaporation rates actually often tend to be larger for the latter. Even if the Marangoni convection tends to enhance the transfer, evaporative cooling acts in the opposite sense by reducing the local volatility. Furthermore, in the cases with the electric field and/or buoyancy (normal gravity), the Marangoni convection actually acts in the opposite direction to electroconvection and/or gravity currents, thus reducing the efficiency of a convective mass transfer enhancement. Notwithstanding, for a larger droplet in microgravity and in the absence of an electric field, the Marangoni convection becomes a so strong sole convective enhancement factor that the evaporation rate of a real droplet overtakes and eventually exceeds the one of an isothermal droplet. It is worth noting that the evaporation rates computed for an isothermal droplet are always larger than the corresponding pure-diffusion results, due to Stefan flow present for the former and absent for the latter. While buoyancy (normal gravity) is well-known to be a strong convective enhancing factor (of the order of 60% in the present study), the electric field in microgravity here turned out to be a more modest yet still consistent enhancer (by the order of 20%). Finally, as far as the runs with an electric field in microgravity are concerned, one can mention that the evaporation rates for a spherical-cap droplet are found to be only slightly (by a few percent) different from those for a droplet of the same volume with the shape deformed by the electric field ("e-shape").

Vapor interferometry together with simulations has also permitted an inquiry into a number of malfunctions detected in the ARLES experiment. The most important of them concerned the measured evaporation rates in microgravity (0.087 and 0.109 μL/s without and with an electric field, respectively), which turned out to be quite lower than in simulations (∼0.14 μL/s and 0.17 μL/s, respectively), whereas there was a fairly good agreement for normal-gravity runs. It was concluded that this was most likely related to leaking into the droplet from a very considerable dead volume of the liquid in the injection system occurring during the sounding-rocket experiment.

A new edition of the ARLES experiment, ARLES-II, is currently under way, where these and other shortcomings are sought to be corrected. It is our belief that the insights obtained in this paper should open the field for the development of a range of evaporation enhancement devices to be used in space, focused on tailoring the flows in the vapor cloud.

■ ASSOCIATED CONTENT

Supporting Information

The Supporting Information is available free of charge at https://pubs.acs.org/doi/10.1021/acs.langmuir.3c00689.

Additional details on gas mixture viscosity, e-shape fitting, droplet volume evolution used in simulation, reference results from the literature for the evaporation rate, and malfunction analysis (PDF)

https://doi.org/10.1021/acs.langmuir.3c00689
Langmuir XXXX, XXX, XXX−XXX

Fringe pattern evolution for the droplet 7DPμg in experiment (AVI)
Fringe pattern evolution for the droplet 7DPμg in numerical simulations (AVI)
Fringe pattern evolution for the droplet 8DPμgEF in experiment (AVI)
Fringe pattern evolution for the droplet 8DPμgEF in numerical simulations (AVI)
Fringe pattern evolution for the droplet 3DP1g in experiment (AVI)
Fringe pattern evolution for the droplet 3DP1g in numerical simulations (AVI)
Fringe pattern evolution for the droplet 4DP1gEF in experiment (AVI)
Fringe pattern evolution for the droplet 4DP1gEF in numerical simulations (AVI)
Fringe pattern evolution for the droplet 6DPμgEF in experiment (AVI)
Fringe pattern evolution for the droplet 6DPμgEF in numerical simulations (AVI)

AUTHOR INFORMATION

Corresponding Author

Alexey Y. Rednikov − *TIPs Laboratory, Université libre de Bruxelles, B-1050 Brussels, Belgium;* orcid.org/0000-0003-4221-6961; Email: alexey.rednikov@ulb.be

Authors

Sam Dehaeck − *TIPs Laboratory, Université libre de Bruxelles, B-1050 Brussels, Belgium;* orcid.org/0000-0002-3964-102X

Hatim Machrafi − *Institut de Physique, Université de Liège, B-4000 Liège, Belgium*

Alekos Ioannis Garivalis − *DESTEC, University of Pisa, I-56122 Pisa, Italy;* orcid.org/0000-0003-1981-0882

Paolo Di Marco − *DESTEC, University of Pisa, I-56122 Pisa, Italy*

Senthil Kumar Parimalanathan − *TIPs Laboratory, Université libre de Bruxelles, B-1050 Brussels, Belgium;* orcid.org/0000-0001-7537-0020

Pierre Colinet − *TIPs Laboratory, Université libre de Bruxelles, B-1050 Brussels, Belgium*

Complete contact information is available at: https://pubs.acs.org/10.1021/acs.langmuir.3c00689

Notes

The authors declare no competing financial interest.

ACKNOWLEDGMENTS

The present work was carried out in the framework of the European Space Agency research project AO-1999-110: EVAPORATION. We thank the ARLES Science Team: Dr. C.S. Iorio (coordinator), MRC/CREST − Université libre de Bruxelles, University of Pisa, IUSTI − Aix-Marseille University, TIPs − Université libre de Bruxelles, Université de Liège, University of Alberta, Technical University of Darmstadt, University of Edinburgh, University of Loughborough, Trinity College Dublin, Institute of Mechanics − Chinese Academy of Sciences, and Kutateladze Intitute of Thermophysics − Siberian Branch of the Russian Academy of Sciences. We are grateful to Dr. D. Mangini, Dr. B. Toth and Dr. A. Verga (ESA coordinators) and the Swedish Space Corporation (technical realization of the experiment). The Belgian teams acknowledge the funding from the BELSPO PRODEX Evaporation project. PC acknowledges the funding from the Fonds de la Recherche Scientifique − FNRS (Research Director Position).

REFERENCES

(1) Di Marzo, M.; Tinker, S. Evaporative cooling due to a sparse spray. *Fire Safety Journal* **1996**, *27*, 289−303.
(2) Kim, J. Spray cooling heat transfer: The state of the art. *International Journal of Heat and Fluid Flow* **2007**, *28*, 753−767.
(3) Wijshoff, H. Drop dynamics in the inkjet printing process. *Curr. Opin. Colloid Interface Sci.* **2018**, *36*, 20−27.
(4) David, S.; Sefiane, K.; Tadrist, L. Experimental investigation of the effect of thermal properties of the substrate in the wetting and evaporation of sessile drops. *Colloids Surf., A* **2007**, *298*, 108−114.
(5) Dunn, G.; Wilson, S.; Duffy, B.; David, S.; Sefiane, K. The strong influence of substrate conductivity on droplet evaporation. *J. Fluid Mech.* **2009**, *623*, 329−351.
(6) Fabien, G.; Antoni, M.; Sefiane, K. Use of IR thermography to investigate heated droplet evaporation and contact line dynamics. *Langmuir* **2011**, *27*, 6744−6752.
(7) Lopes, M.; Bonaccurso, E.; Gambaryan-Roisman, T.; Stephan, P. Influence of the substrate thermal properties on sessile droplet evaporation: Effect of transient heat transport. *Colloids Surf., A* **2013**, *432*, 64−70.
(8) Gibbons, M.; Di Marco, P.; Robinson, A. Local heat transfer to an evaporating superhydrophobic droplet. *Int. J. Heat Mass Transfer* **2018**, *121*, 641−652.
(9) Kelly-Zion, P.; Pursell, C.; Booth, R.; Van Tilburg, A. Evaporation rates of pure hydrocarbon liquids under the influences of natural convection and diffusion. *Int. J. Heat Mass Transfer* **2009**, *52*, 3305−3313.
(10) Sefiane, K.; Wilson, S.; David, S.; Dunn, G.; Duffy, B. On the effect of the atmosphere on the evaporation of sessile droplets of water. *Phys. Fluids* **2009**, *21*, 062101.
(11) Dehaeck, S.; Rednikov, A.; Colinet, P. Vapor-based interferometric measurement of local evaporation rate and interfacial temperature of evaporating droplets. *Langmuir* **2014**, *30*, 2002−2008.
(12) Deegan, R.; Bakajin, O.; Dupont, T.; Huber, G.; Nagel, S.; Witten, T. Capillary flow as the cause of ring stains from dried liquid drops. *Nature* **1997**, *389*, 827−829.
(13) Popov, Y. Evaporative deposition patterns: Spatial dimensions of the deposit. *Phys. Rev. E* **2005**, *71*, 036313.
(14) Tsoumpas, Y.; Dehaeck, S.; Galvagno, M.; Rednikov, A.; Ottevaere, H.; Thiele, U.; Colinet, P. Nonequilibrium Gibbs' criterion for completely wetting volatile liquids. *Langmuir* **2014**, *30*, 11847−11852.
(15) Kelly-Zion, P.; Pursell, C.; Hasbamrer, N.; Cardozo, B.; Gaughan, K.; Nickels, K. Vapor distribution above an evaporating sessile drop. *Int. J. Heat Mass Transfer* **2013**, *65*, 165−172.
(16) Carle, F.; Sobac, B.; Brutin, D. Experimental evidence of the atmospheric convective transport contribution to sessile droplet evaporation. *Appl. Phys. Lett.* **2013**, *102*, 061603.
(17) Somasundaram, S.; Anand, T.; Bakshi, S. Evaporation-induced flow around a pendant droplet and its influence on evaporation. *Phys. Fluids* **2015**, *27*, 112105.
(18) Kumar, S.; Medale, M.; Di Marco, P.; Brutin, D. Sessile volatile drop evaporation under microgravity. *npj Microgravity* **2020**, *6*, 37.
(19) Garivalis, A.; Di Marco, P.; Dehaeck, S.; Rednikov, A.; Colinet, P. Experimental study on evaporation of droplets in microgravity and in the presence of electric field. *J. Phys.: Conf. Ser.* **2022**, *2177*, 012047.
(20) Liimatainen, V.; Sariola, V.; Zhou, Q. Controlling liquid spreading using microfabricated undercut edges. *Adv. Mater.* **2013**, *25*, 2275−2278.
(21) Shevchenko, V.; Mialdun, A.; Yasnou, V.; Lyulin, Y.; Ouerdane, H.; Shevtsova, V. Investigation of diffusive and optical properties of

vapour-air mixtures: The benefits of interferometry. *Chem. Eng. Sci.* **2021**, *233*, 116433.
(22) Machrafi, H.; Sadoun, N.; Rednikov, A.; Dehaeck, S.; Dauby, P.; Colinet, P. Evaporation rates and Bénard-Marangoni supercriticality levels for liquid layers under inert gas flow. *Microgravity Sci. Technol.* **2013**, *25*, 251−265.
(23) Tsoumpas, Y.; Dehaeck, S.; Rednikov, A.; Colinet, P. Effect of Marangoni flows on the shape of thin sessile droplets evaporating into air. *Langmuir* **2015**, *31*, 13334−13340.
(24) Pendrill, L. Refractometry and gas density. *Metrologia* **2004**, *41*, S40−S51.
(25) O'Brien, R.; Saville, P. Investigation of liquid drop evaporation by laser interferometry. *Langmuir* **1987**, *3*, 41−45.
(26) Kreis, T. Digital holographic interference-phase measurement using the Fourier-transform method. *J. Opt. Soc. Am. A* **1986**, *3*, 847−855.
(27) Takeda, M.; Ina, H.; Kobayashi, S. Fourier-transform method of fringe-pattern analysis for computer-based topography and interferometry. *J. Opt. Soc. Am. A* **1982**, *72*, 156−160.
(28) Hansen, E. Space-domain inversion of the incomplete Abel transform. *J. Opt. Soc. Am. A* **1992**, *9*, 2126−2137.
(29) Kelly-Zion, P.; Pursell, C.; Vaidya, S.; Batra, J. Evaporation of sessile drops under combined diffusion and natural convection. *Colloids Surf., A* **2011**, *381*, 31−36.
(30) Hu, H.; Larson, R. Analysis of the effects of Marangoni stresses on the microflow in an evaporating sessile droplet. *Langmuir* **2005**, *21*, 3972−3980.
(31) Girard, F.; Antoni, M.; Faure, S.; Steinchen, A. Evaporation and Marangoni driven convection in small heated water droplets. *Langmuir* **2006**, *22*, 11085−11091.
(32) Ristenpart, W.; Kim, P.; Domingues, C.; Wan, J.; Stone, H. Influence of substrate conductivity on circulation reversal in evaporating drops. *Phys. Rev. Lett.* **2007**, *99*, 234502.
(33) Saville, D. Electrohydrodynamics: The Taylor-Melcher leaky dielectric model. *Annu. Rev. Fluid Mech.* **1997**, *29*, 27−64.
(34) Garivalis, A. Effect of an external electric field on bubbles and sessile drops in microgravity environment: Interfacial dynamics and heat transfer. *Ph.D. thesis*, University of Pisa, 2022.
(35) Melcher, J.; Taylor, G. Electrohydrodynamics: A review of the role of interfacial shear stresses. *Annu. Rev. Fluid Mech.* **1969**, *1*, 111−146.
(36) Bird, R.; Steward, W.; Lightfoot, E. *Transport Phenomena*; Wiley, 2006; p 928.
(37) Machrafi, H.; Dauby, P. Impact of initial conditions and gas dynamics on the evaporation of a sessile droplet in microgravity and on-ground explained by a numerical model. *Int. J. Heat Mass Transfer* **2023**, *204*, 123867.

https://doi.org/10.1021/acs.langmuir.3c00689
Langmuir XXXX, XXX, XXX−XXX